Aerodynamic drag determination of a full-scale cyclist mannequin from largescale PTV measurements

Sciacchitano, Andrea; Terra, Wouter; Shah, Yash

Publication date
2018

Document Version
Final published version

Published in
Proceedings of the 19th international symposium on application of laser and imaging techniques to fluid mechanics

Citation (APA)
Sciacchitano, A., Terra, W., & Shah, Y. (2018). Aerodynamic drag determination of a full-scale cyclist mannequin from largescale PTV measurements. In *Proceedings of the 19th international symposium on application of laser and imaging techniques to fluid mechanics*

Aerodynamic drag determination of a full-scale cyclist mannequin from large-scale PTV measurements

A. Sciacchitano[1,*], W. Terra[1], Y. H. Shah[2]
1: Dept. of Aerospace Engineering, Delft University of Technology, The Netherlands
2: Dept. of Mechanical and Mechatronics Engineering, University of Waterloo, Ontario Canada
* Correspondent author: a.sciacchitano@tudelft.nl

Keywords: Aerodynamic drag, PIV wake rake, human-scale PTV, helium-filled soap bubbles, cycling aerodynamics

ABSTRACT

Large-scale Particle Tracking Velocimetry (PTV) measurements are conducted in the wake of a full-scale cyclist model in time-trial position at freestream velocities between 12.5 and 15 m/ s, corresponding to Reynolds numbers of the order of 5×10^5. Lagrangian particle tracking is employed to determine the velocity and static pressure statistics in the wake plane, showing good agreement with previous results reported in literature. The aerodynamic drag is estimated from the large-scale PTV measurements invoking the conservation of momentum in a control volume enclosing the model (PIV wake rake approach). The estimated drag follows the expected quadratic increase with increasing freestream velocity. The accuracy of the drag estimate is evaluated by comparison to state-of-the-art force balance measurements, resulting in a resolution of the PIV wake rake approach of 30 drag counts. The three terms composing the overall drag force, associated with the time-average streamwise velocity, its fluctuations and the time-averaged pressure, respectively, are evaluated separately, demonstrating that the contribution of the pressure term is negligible and the resistive force is dominated by the time-average streamwise momentum deficit.

1. Introduction

Determination of the aerodynamic loads is relevant in many fluid dynamic applications, e.g. for the fuel-efficient design of air and ground transportation systems, the safe structural design of wind turbines, and the maximization of performances in elite speed sports such as cycling and skating. To quantify the aerodynamic loads, wind tunnel measurements are typically conducted on models immersed in a homogeneous stream of air, measuring the aerodynamic forces and moments acting on the model using a six component force balance (e.g. Zdravkovich 1998, Tropea et al. 2007). Due to their high resolution (up to 0.0003% of the full scale load, Tropea et al. 2007), these balance systems are nowadays considered as standard tool especially for measurements in industrial wind tunnels. Nevertheless, balance measurements are regarded as "blind", in the sense that they do not provide any insight in the flow field and flow structures generating the aerodynamic loads. Alternatively, the aerodynamic loads can be evaluated using wake rakes, invoking the conservation of momentum across a control volume containing the model and measuring the total and static pressure in the wake of the model (Betz 1925; Jones 1936; Goett 1938; Somers 1997, among others). In contrast to balance measurements, the wake

rake approach provides not only the aerodynamic drag, but also information on the pressure and velocity field and momentum deficit in the wake of the model, yielding a deeper insight into the generation of the total resistive force (e.g. Maskell 1973, Hucho and Sovran 1993).

Thanks to its non-intrusive nature and whole-field measurement capability, in the last two decades Particle Image Velocimetry (PIV) has been used extensively as a viable alternative to the pressure probe wake rakes, for loads determination from wake velocity data. Lin and Rockwell (1996) and successively Unal et al. (1997) conducted PIV measurements in the wake of a two-dimensional cylinder to characterize its unsteady lift coefficient at Re = 3,780. Similarly, Kurtulus et al. (2007) made use of time-resolved PIV to quantify the unsteady aerodynamic forces of a square-section cylinder at Re = 4,890. Using PIV velocity data and the control volume approach, van Oudheusden et al. (2006) characterized the time-average aerodynamic forces (lift, drag and pitching moment) of an airfoil; the authors reported discrepancies between the drag coefficient measured from PIV and the conventional wake-rake approach of 1 drag count (or $\Delta C_D=10^{-3}$). Ragni et al. (2009) proved the feasibility of the PIV wake rake for drag determination of a transonic airfoil at Mach = 0.6. In a successive work, the authors extended the use of the PIV wake rake to moving objects for the determination of the aerodynamic loads on an aircraft propeller blade (Ragni et al. 2011). A detailed review of loads estimation approaches from PIV measurements has been recently carried out by Rival and van Oudheusden (2017).

Despite the popularity of the PIV wake rake for measuring the time-average and instantaneous loads and investigation of the governing flow fields, its application has been limited to relatively small-sized wind tunnel models (typical characteristic length of the order of 10 cm) due to the limited domain of conventional PIV measurements (Raffel et al. 2018). This is largely ascribed to the low scattering efficiency of conventional micrometric flow tracers. The introduction of sub-millimeter Helium-filled soap bubbles (HFSB) as flow tracers for PIV measurements (Bosbach et al. 2009; Scarano et al. 2015) allowed an increase in measurement volume, which has mainly been exploited for volumetric PIV measurements. Caridi et al. (2016) made use of large-scale tomographic PIV over a volume of 12 liters to investigate the flow field at the tip of a vertical axis wind turbine blade. By conducting large-scale PTV measurements and solving the Poisson equation for pressure, Schneiders et al. (2016) measured the instantaneous volumetric pressure in the wake of a truncated cylinder over a volume of about 6 liters. Loads determination from large-scale PIV has been attempted for the first time by Terra et al. (2017), estimating the drag coefficient of a transiting sphere at Re = 10,000. However, load determination from large-scale PIV in wind tunnels has been hampered, firstly, by the limited HFSB tracers concentration achieved so far, which has been below 1 bubble/ cm^3 (Caridi et al. 2016) and, secondly, by the limited size of the seeded stream tube cross-section (~0.1 m^2, Caridi et al. 2016; Jux et al. 2018).

The present work aims at assessing the feasibility of using a large-scale PIV wake rake for the determination of the aerodynamic drag on a three-dimensional human-scale wind tunnel model. For this purpose, Lagrangian particle tracking is employed to obtain the velocity field in a plane of approximately 1.6 m^2 in the wake of a full-scale cyclist mannequin, demonstrating the PIV wake rake approach over a human-scale model on a fully three-dimensional, unsteady and highly complex flow. The obtained time-average flow topology is presented and validated against literature. Furthermore, for the first time the distribution of streamwise velocity fluctuations and pressure coefficient in the wake of a cyclist model are presented and discussed. Finally, the accuracy of the PIV wake rake approach for drag estimation is evaluated by varying freestream velocity and by comparison with state-of-the-art balance measurements.

2. Theoretical background

Consider a body in relative motion with respect to a fluid. In the incompressible flow regime, the instantaneous drag of the object can be determined invoking the conservation of momentum in a control volume enclosing the body (Rival and van Oudheusden 2017):

$$D(t) = -\rho \iiint_V \frac{\partial u}{\partial t} dV + \iint_{S_{wake}} (U_\infty - u) u dS + \iint_{S_{wake}} (p_\infty - p) dS \tag{1}$$

where V is the control volume, S_{wake} is the downstream boundary of the control volume, ρ, p_∞ and U_∞ are the air density, freestream velocity and freestream static pressure, respectively; p and u are the static pressure and streamwise velocity at the location S_{wake}, as illustrated in Fig. 1.

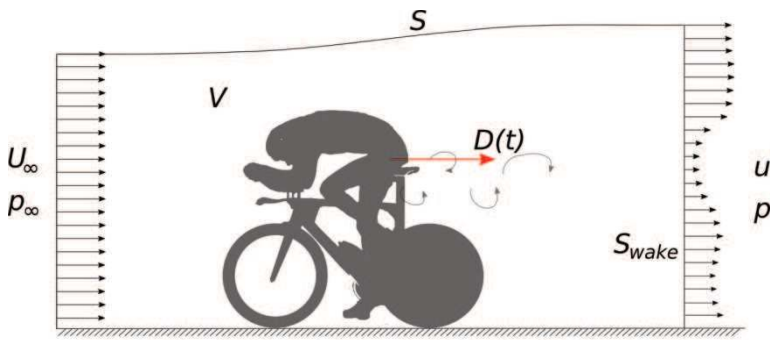

Fig. 1 Schematic of the control volume approach to determine the aerodynamic drag of an object.

Applying Reynolds decomposition to velocity and pressure and averaging both sides of equation (1), the time-averaged drag is obtained (Terra et al. 2017):

$$\overline{D} = \rho \iint_{S_{wake}} (U_\infty - \overline{u}) \overline{u} dS - \rho \iint_{S_{wake}} \overline{u'^2} dS + \iint_{S_{wake}} (p_\infty - \overline{p}) dS \tag{2}$$

where $\overline{u}$ is the time-average streamwise velocity component, u' the fluctuating streamwise velocity component and $\overline{p}$ the time-average static pressure. In the reminder of this work, the first, second and third term at the right hand side of equation (2) are referred to as the momentum term, the Reynolds stress term and the pressure term, respectively. Equation (2) allows evaluating the time-average aerodynamic drag from velocity and pressure statistics in the wake of the wind tunnel model. The time-averaged static pressure is computed from the PIV data by solving the Poisson equation with appropriate boundary conditions (van Oudheusden 2013).

The accuracy of the drag estimation via the PIV wake rake approach is assessed via direct comparison with state-of-the-art balance measurements. The measurements are repeated in a narrow range of Reynolds numbers, where the drag coefficient is assumed to be constant. The drag resolution of the PIV wake rake is evaluated as:

$$\Delta C_D = \sqrt{\frac{1}{N}\sum_{i=1}^{N}(\overline{C_{D_{i,PIV}}} - \overline{C_{D_{i,bal}}})^2} \tag{3}$$

where $\overline{C_{D_{i,PIV}}}$ and $\overline{C_{D_{i,bal}}}$ are the time-average drag coefficients from PIV wake rake and balance system, respectively, and N is the number of repeated measurements at different freestream velocities.

3. Experimental apparatus and procedure

3.1 Wind tunnel model

The experiments are conducted in the Open Jet Facility (OJF) of the Aerodynamics Laboratories at the Delft University of Technology. This atmospheric closed-loop, open-jet wind tunnel has an octagonal cross-section of 2.85×2.85 m^2 with a contraction ratio of 3:1, that allows the generation of a homogeneous jet at speeds between 4 to 35 m/ s with 0.5% turbulence intensity (Lignarolo et al. 2014). The wind tunnel model consists of a rigid-body full-scale cyclist mannequin seated on a time-trial bike. The latter is supported at the front and rear axis, as illustrated in Fig. 2, with the front wheel centerline located 1 m downstream of the OJF contraction exit. The mannequin, wearing a long-sleeve Etxeondo time-trial suit along with a Giant time trial helmet (season 2016), is manufactured from thermoplastic polyester by additive manufacturing after three-dimensional scanning of an elite cyclist in time-trial position (Van Tubergen et al. 2017). The legs of the mannequin are in asymmetric position (left leg stretched and right leg bended) relating to a 75° crank angle (Fig. 2). The hip width W, torso length T and frontal area A of the model are 0.365 m, 0.600 m and 0.32 m^2, respectively. More details of the mannequin dimensions are

provided in the work of Jux et al. (2018). A 4.9 m long and 3.0 m wide wooden table, elevated 20 cm above the wind tunnel contraction exit, reduces the boundary layer thickness interacting with the model.

Fig. 2 Wind tunnel model and PIV seeding system.

3.2 PTV system

The flow field in the wake of the cyclist model is measured by Lagrangian particle tracking with neutrally buoyant helium-filled soap bubbles (HFSB) as flow tracers. The latter have a diameter of approximately 300 μm (Scarano et al. 2015) and are introduced into the flow by an in-house developed seeding rake installed on a two-axis traversing system at the wind tunnel contraction's exit (Fig. 2). 80 HFSB generators are integrated into the four-wing seeding rake with a vertical and horizontal pitch of 25 mm and 50 mm, respectively. The rake is installed 85 cm upstream of the front wheel's axis and releases approximately 2×10^6 bubbles per second seeding a streamtube of 20×50 cm^2 cross-section in the freestream. The resulting seeding concentration at a freestream velocity of 14 m/ s is estimated at 1.4 tracer/ cm^3 (Caridi et al. 2016). The flow rates of helium, air and bubble fluid solution are regulated via a Fluid Supply Unit from LaVision GmbH. In order to seed the entire wake of the model, measurements are repeated at 15 different positions of the seeding rake, 5 along the horizontal direction and 3 along the vertical direction. Two meters downstream of the four-wing seeding rake, the turbulence intensity of the OJF freestream jet is increased from 0.5% to 1.9%, while the mean flow remains unaltered (Jux et al. 2018).

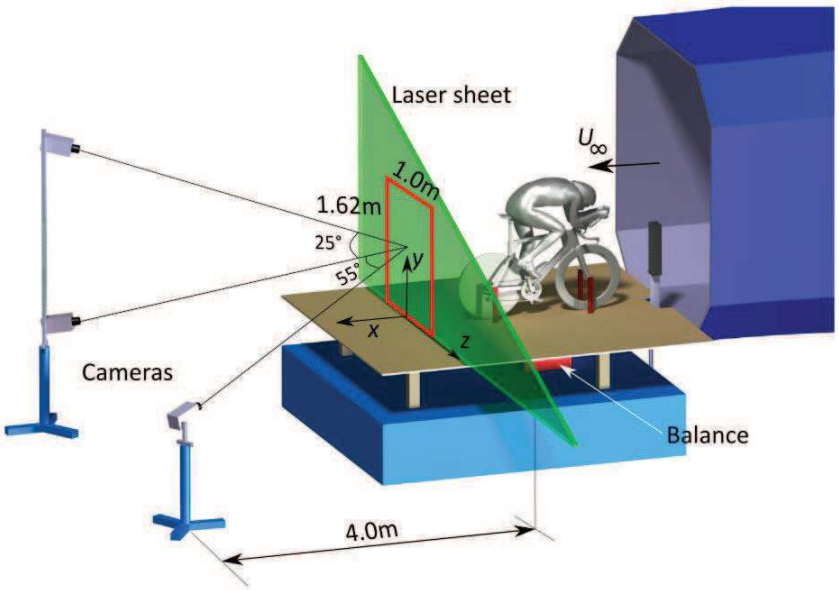

Fig. 3 Schematic representation of the experimental setup.

Collimated light is provided by a Continuum Mesa PIV 532-120-M laser (Nd:YAG diode pumped laser, pulse energy of 18 mJ at 1 kHz) illuminating a 5 cm thick plane, 80 cm downstream of the trailing edge of the saddle of the bike (see Fig. 3). Time-resolved images are acquired by three Photron FastCAM SA1 cameras (CMOS sensor, 12 bit, 20 μm pixel pitch, 1,024×1,024 pixels at full resolution) over a region of approximately 1.0×1.6 m^2. The cameras are located about four meter downstream of the model, two meters from the open jet's central axis (Fig. 3). The cameras are equipped with 50 mm Nikkor objectives with an aperture set to f/ 4 and tilt adapters to satisfy the Scheimpflug condition. The optical magnification is equal to 0.0125, resulting in a digital image resolution of 1.6 mm/ px. For the geometrical camera calibration, an in-house developed double-plane calibration target of 1.2 m × 1.2 m is placed vertically at two locations, 5 cm upstream and 5 cm downstream of the measurement plane. The target contains a total of 156 circular dots of 8 mm diameter per plane, distributed over 12 rows and 13 columns with a pitch of 9 cm in both vertical and horizontal direction. The offset between the two planes is 2 cm; the dots of the two planes are staggered by 4.5 cm in both the vertical and horizontal directions.

3.3 PTV measurement procedure

The images are recorded in short bursts of 11 images at 4 kHz acquisition frequency resulting in a mean track length of five samples which is approximately independent of the transverse location on the wake plane. Particle streaks, obtained as the maximum image intensity over the 11 subsequent images of a burst, in the center of the model's wake and the freestream are depicted in Fig. 4-left and right, respectively. The number of particles per pixel (ppp) varies

between 0.04 and 0.1 depending on the seeder position, being the highest in the freestream (where the seeded streamtube is mainly unaffected by the wake of the model) and the lowest in the cyclist's wake due to the mixing of the seeded flow with un-seeded air. The average particle intensity is rather independent of the seeder position and is equal to 200 counts over a background intensity of about 20 counts, resulting in an image signal-to-noise ratio of 10. For each position of the seeding generator, 480 bursts are acquired with 0.1 s separation between two successive bursts to obtain a statistical ensemble of uncorrelated particle tracks. Image acquisition and processing is conducted with DaVis 8.4 from LaVision GmbH.

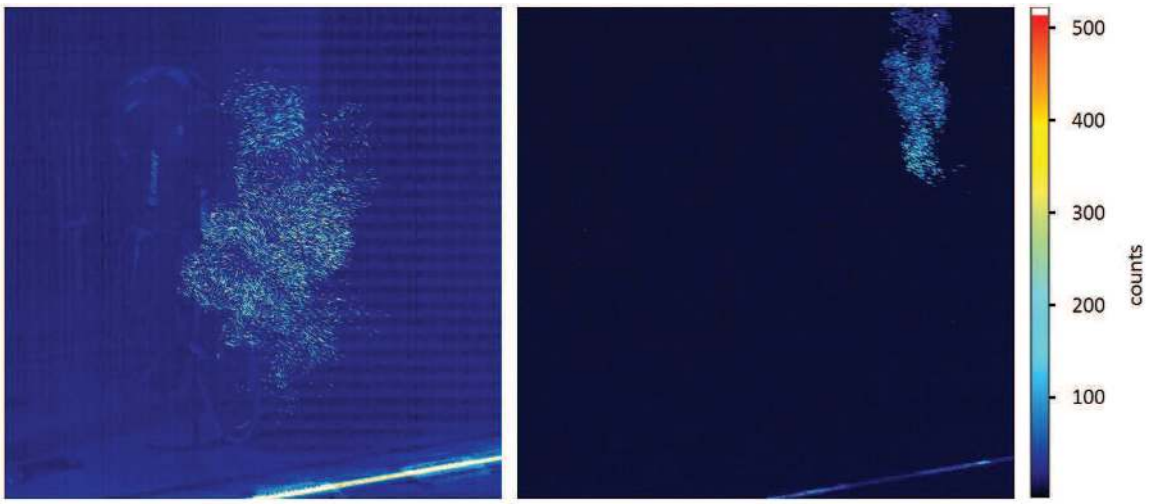

Fig. 4 HFSB seeding in the wake of the model. Particle streaks in the central wake without image pre-processing (left) and in the freestream area after image pre-processing by time-average intensity subtraction (right).

3.4 Force balance measurements

Force measurements are carried out with a six-component balance designed, manufactured and calibrated by the Dutch Aerospace Laboratory (NLR). Under simultaneous loading of all six components (three forces and three moments), the balance is capable of measuring loads up to 250 N in the streamwise direction with a maximum uncertainty of 0.06% (Alons 2008). The balance is mounted directly under the ground plate, shielded from the air below the plate, and connected to the bike supports. The balance measurements are conducted at each position of the seeding rake; the acquisition frequency is set to 2 kHz and the observation time is 30 seconds.

Finally, the PIV and force balance measurements are repeated at five different freestream velocities between 12.5 m/ s and 15 m/ s, corresponding to Re = 5×10^5 to 6×10^5 based on the torso length.

3.5 PTV data reduction

The acquired images are pre-processed by subtraction of the time-averaged intensity of each burst to remove background noise (see Fig. 4-right) and are then processed with the Shake-The-

Box algorithm (STB; Schanz et al. 2016) yielding Lagrangian particle tracks. Particle tracks of single image bursts obtained at the 15 different locations of the seeding rake are depicted in Fig. 5 by separate color illustrating the extent of overlap of tracks from different seeder positions.

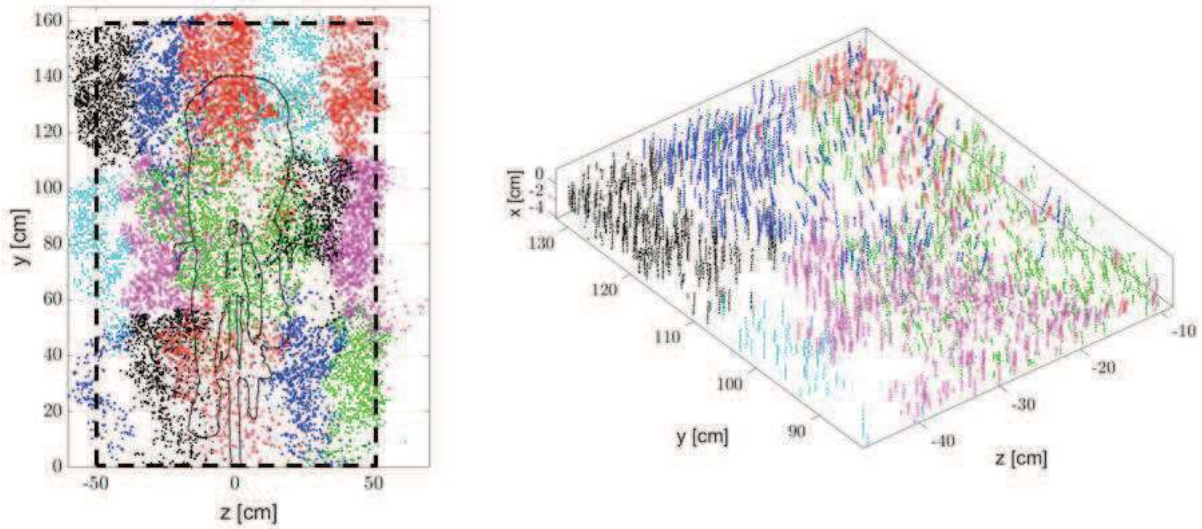

Fig. 5 Lagrangian particle tracks in the wake of the model from a single image burst (different colors represent the different seeder locations).

Velocity statistics (time-average and fluctuations root-mean-square) is computed from the Lagrangian velocity ensemble within bins of size 5×4×4 cm^3 with 75% overlap in all directions (Agüera et al. 2016). The resulting velocity field is defined on a Cartesian grid with a vector pitch of 1 cm along y and z directions. The bin size was determined requiring a minimum number of 25 tracks per bin. A universal outlier detection filter (Westerweel and Scarano, 2005) was applied to the particle velocity data in each bin, to reduce spurious tracks, resulting in an average number of used tracks per bin of approximately 2000. The uncertainty of the obtained velocity data is estimated from the time-average streamwise velocity in the overlapping regions between seeder position. Discrepancies in the order of 5% are 2% are obtained in the wake and the freestream, respectively.

For the computation of the aerodynamic drag according to Eq. (2), apart from the velocity statistics in the wake plane, the freestream velocity U_∞ and static pressure p_∞ are required. The measured freestream velocity $U_{\infty,\mathrm{meas}}$ is obtained as the mean streamwise velocity over the three free boundaries of the wake plane, excluding a region in relative proximity to the floor ($y > 50$ cm). A correction for the jet expansion, ε_S, and the nozzle blockage, ε_N, is applied according to Mercker and Wiedemann (1996):

$$\frac{U_\infty}{U_{\infty,meas}} = 1 + \varepsilon_S + \varepsilon_N \tag{4}$$

with $\varepsilon_S = 0.0018$ and $\varepsilon_N = 0.0132$. The static pressure is obtained solving the Poisson equation for pressure prescribing Neumann conditions on the bottom boundary and Dirichlet conditions with freestream pressure on the three free boundaries. The streamwise gradients of the time-average velocity and its fluctuations are neglected in the pressure reconstruction after estimating that these are two orders of magnitude smaller than the corresponding in-plane gradients.

4. Results

4.1 Wake flow topology

The time-average wake flow topology of the cyclist mannequin is discussed considering the spatial distribution of the streamwise velocity (Fig. 6-left) and vorticity with in-plane vectors (Fig. 6-right). The streamwise velocity contour exhibits two main regions of significant velocity deficit. The first one is located behind the lower back of the mannequin (y ~ 100 cm) slightly towards the left, and features a minimum velocity of u/U_∞~0.6. The lateral asymmetry of this velocity deficit originates from the asymmetric leg position (left leg extended downwards and right leg bent upwards), and is in good agreement with what reported in literature e.g. by Crouch et al. (2014) and Jux et al. (2018). The minimum value of the streamwise velocity is comparatively higher than that measured by Crouch et al. (2014, u/U_∞~ .5) and Jux et al. (2018, u/U_∞~0.35), which in the latter case is attributed to the further upstream location of the measurement plane (x = 30 cm instead of 80 cm), where larger velocity deficits are expected. In the comparison with Crouch et al. (2014), the smaller velocity deficit can be attributed to the combined effect of the smaller angle of attack of trunk of the mannequin (α~5^o for the present model and α =12.5^o for the model used by Crouch et al.), the more aerodynamic position of the head (the head and helmet in the present case do not contribute to the frontal area of the model, while they do in the case of the mannequin used by Crouch et al. 2014), and the higher curvature of the upper back of the present model. The second region of high velocity deficit, with a minimum velocity of about u/U_∞~0.45, is observed downstream of the wheel axis and the drivetrain configuration (y~40 cm), and matches well the work of Crouch et al. (2016) in terms of location and magnitude.

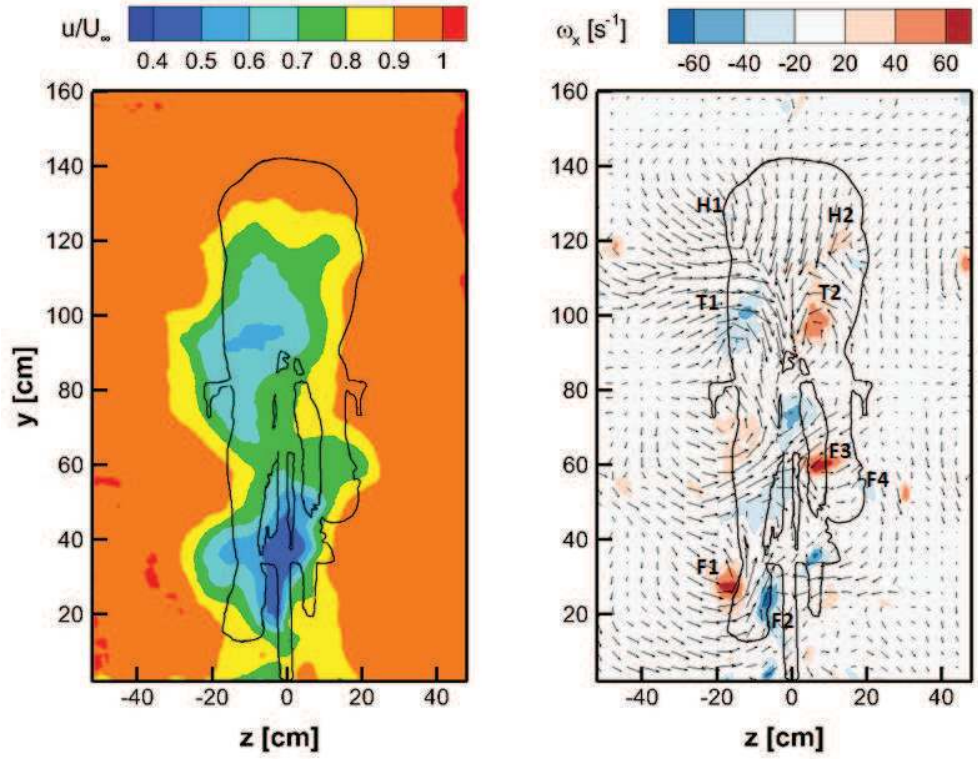

Fig. 6 Time-averaged streamwise velocity component (left) and streamwise vorticity component with in-plane velocity vectors (right). Free-stream velocity equal to 14.5 m/ s (Re = 5.8×10^5).

Fig. 6-right also shows a region of strong downwash behind the curved back of the mannequin (y~120 cm), with a peak vertical velocity of v/U_∞~-0.17 that agrees well with literature (Crouch et al. 2016; Griffith et al. 2014, among others). Two strong counter-rotating vortices (marked T1/ T2) originate from the cyclist's thighs and are fed by the downwash behind the model's back, as also documented in previous literature (Crouch et al., 2014). Besides the vortex pair T1/ T2, other counter-rotating vortex pairs originate from the left foot (marked F1/ F2), producing an up-wash in the foot wake (v/U_∞~-0.12), and from the right foot (marked F3/ F4), which agree well with the robotic-PIV measurements of Jux et al. (2018). The regions of streamwise vorticity emanating from the hips (H1/ H2) are shearing regions rather than vortex regions stemming from the interaction between the downwash motion, discussed before, and the surrounding streamwise motions.

The streamwise velocity fluctuations are illustrated in Fig. 7. The two separated unsteady shear layers behind the left lower leg can be observed (marked S3/ S4), yielding a fluctuation peak of about ~$0.1U_\infty$. These shear layers bend inwards just below the knee due to the strong inward velocity component in this region (y~50; z~-20, Fig. 6-right), possibly resulting from a counter-clockwise streamwise vortex originating from the left knee/ lower leg. Also the outer shear layer originating from the upper part of the extended leg exhibits maximum fluctuations of similar magnitude (y~90 cm and z~-15 cm). Conversely, the streamwise velocity fluctuations behind the

bent leg are comparatively lower, with peaks of about ~0.06 U_∞. The location of counter-rotating streamwise vortex pairs originating from the thighs (T1/ T2 in Fig. 6-right) and the shearing regions (H1/ H2) coincides with two regions of high streamwise velocity fluctuations (T1/ T2 and H1/ H2 in Fig. 7) indicating that these flow structures are unsteady in nature. Hence, the presented time-average streamwise vorticity levels in Fig. 6-right are below the peak values representative for the instantaneous vortex topology. Finally, other local maxima of the streamwise velocity fluctuations appear in the wake of the drivetrain and behind the lower part of the wheel (V-shape area). To the best knowledge of the authors, the spatial distribution of the streamwise fluctuating velocity at the current freestream velocities has not been reported in literature. Crouch et al. (2014) present the spatial distribution of the principle turbulence intensity for the upper part of the wake (y > 70 cm) reporting maximum values around 0.2, which match reasonably well the present findings.

Outside of the wake of the mannequin, the root-mean-square of the streamwise velocity fluctuations reduces significantly, reaching a level of about 4% of the free-stream velocity. With an estimated freestream turbulence level in the wake of the seeding system of 1.9% (Jux et al., 2018), it is argued that about half of the measured free-stream fluctuations value stems from measurement errors of the large-scale PTV system. As a consequence, the contribution of the Reynolds stress term in the expression for the drag (second term in Eq. (2)) is overestimated, thus yielding an underestimation of the aerodynamic drag by approximately 0.15 N.

Fig. 8 depicts the spatial distribution of the pressure coefficient showing the presence of a large high pressure (HP1) region behind the upper back of the cyclist. This overpressure is attributed to the expansion of the flow after passing the curved back of the cyclist. Below this, at around y = 90 cm, the flow has separated over the lower back of the cyclist, resulting in a separated region where the local static pressure is below the free-stream pressure (LP1). Furthermore, a second low pressure region takes place because of the flow separation between the left foot and the rear wheel (LP2). The overall distribution matches well to that obtained by Blocken et al. (2013) solving the steady Reynolds-averaged Navier–Stokes equations, despite the small differences in model geometry and crank angle (symmetric leg position instead of the present asymmetric case). Despite the distinguished contours, the spatial variations of the pressure coefficient are small (up to 0.03 between minimum and maximum C_p in the wake plane) and the pressure in most of the domain equals the freestream pressure, suggesting that the contribution of the pressure term to the aerodynamic drag evaluated by Equation (2) is small, which is discussed in more detail in the next section.

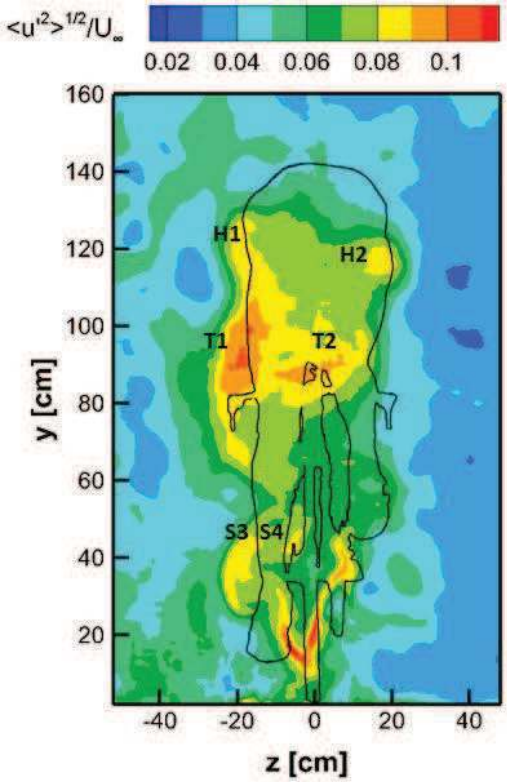

Fig. 7 Streamwise velocity fluctuations in the wake plane at free-stream velocity of 14.5 m/ s (Re = 5.8×10^5).

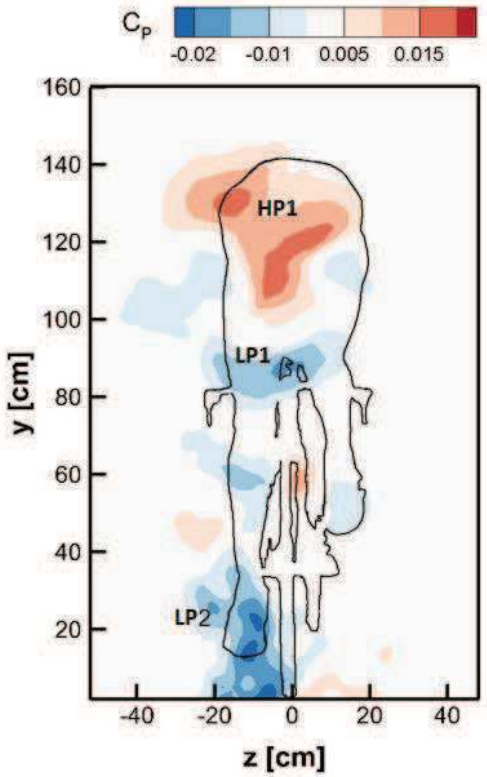

Fig. 8 Time-averaged pressure coefficient in the wake plane at free-stream velocity of 14.5 m/ s (Re = 5.8×10^5).

The flow topology at different freestream velocities is addressed in Fig. 9. The present experiment is repeated within a narrow range of freestream velocities (12.5 m/ s < U_∞ < 15 m/ s) where the drag coefficient is constant (Grappe 2009) and, hence, the flow topology is expected to remain unaltered. The contours of 90% of u/U_∞ at five freestream speeds coincide well and discrepancies of about 5% in non-dimensional streamwise velocity are observed between the different freestream conditions, indicating a good level of repeatability of the experiment.

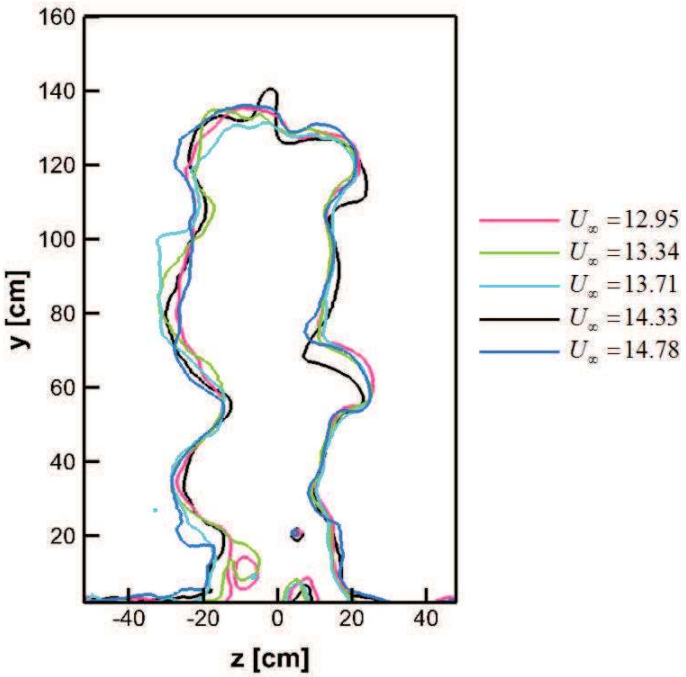

Fig. 9 Contours of 90% u/U_∞ at the different freestream velocities.

4.2 Drag estimation

Considering the unaltered flow topology at the different freestream velocities, the drag coefficient of the cyclist can be assumed constant and the aerodynamic drag is expected to scale quadratically with increasing velocity. Therefore, despite the narrow range of freestream velocities, the drag force is expected to increase by almost 50%. This expected increase is clearly observed in Fig. 10 depicting the resistive force at five freestream velocities. A quadratic fit ($D = 0.14U_\infty^2$) through the five data points and (0,0) is also included. The accuracy of the obtained drag is estimated from the root-mean-square of the residuals between the measured data and the quadratic fit, and is equal to $\Delta D = 1.2$ N.

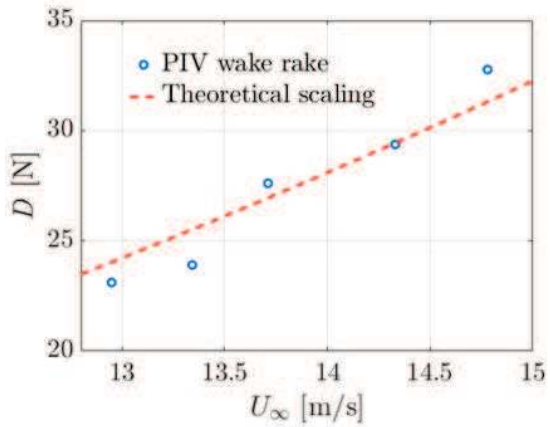

Fig. 10 Time-averaged aerodynamic drag at five freestream velocities including a quadratic fit to the five data points.

The accuracy of the drag estimation, or drag resolution, is evaluated comparing the drag coefficients obtained with the PIV wake rake with those obtained with the force balance. The

balance measurements depicted in Fig. 11-left (dashed-red) show that the drag coefficient is approximately constant in the narrow range of free-stream velocities, with variations of about 1.5%. The error bars on the time-average drag coefficient indicate the uncertainty of the mean value at 95% confidence level. In contrast to the measurements by force balance, the variations observed in the drag coefficient obtained from the PIV wake rake are significantly larger (Fig. 11-left solid-blue), illustrating the higher measurement uncertainty of this technique. Fig. 11-right (dashed-red) shows the error in the drag coefficient measured by PIV wake-rake approach relative to that obtained by balance measurements, which varies between 0.75 and 6.5%. Using Eq. (3), a drag resolution of the PIV wake rake of $\Delta C_D = 0.03$ or 30 drag counts, is estimated (Fig. 11-right solid-blue line).

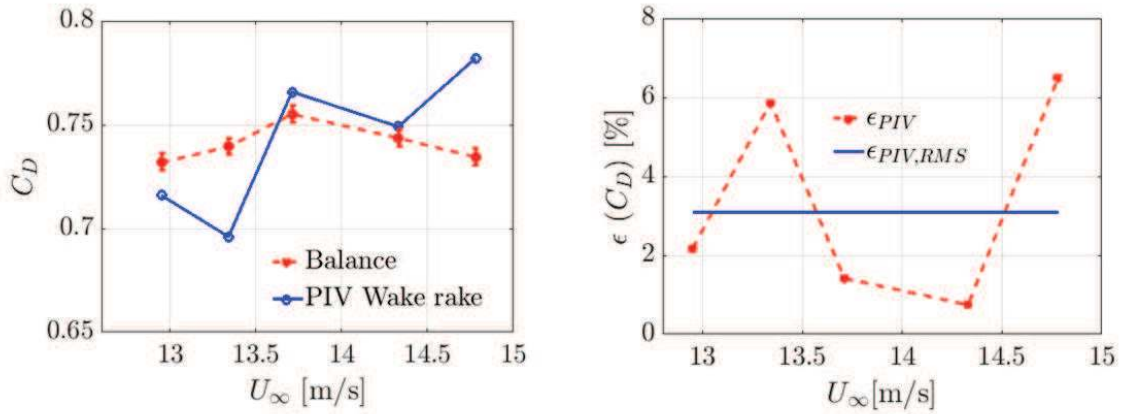

Fig. 11 Aerodynamic drag coefficient from the PIV wake rake vs force balance (left) and the relative error of the PIV wake rake value as a percentage of the balance data (right).

Finally, the separate contributions of the momentum term, Reynolds stress term and pressure term (Eq. (2)) to the overall aerodynamic drag are depicted in Fig. 12. The contribution of the latter is approximately zero at all freestream conditions, which was expected from the small values of the pressure coefficient in the wake plane (Fig. 8). Hence, the pressure reconstruction can be omitted in future cyclist drag estimations with a wake plane downstream position x/ L≥2.2, where L=W (being W the hip width) is the characteristic length scale representative for the wake topology, thus significantly simplifying the evaluation of the aerodynamic drag. The Reynolds stress term consistently contributes to approximately 5% of the drag and cannot be neglected. Finally, the momentum term dominates the air resistance accounting for the remaining 95%.

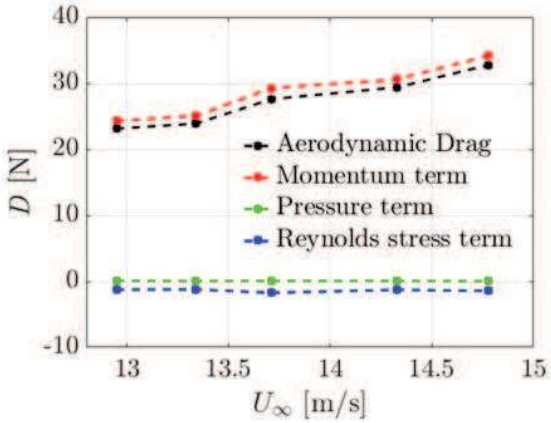

Fig. 12 Time-average aerodynamic drag from the PIV wake rake at five freestream velocities including the individual momentum, pressure and Reynolds stress term.

5. Conclusions

Large-scale PTV measurements are achieved at Reynolds numbers of approximately 5×10^5 in a thin volume of $5\times100\times160$ cm^3, spanning the entire wake of a cyclist mannequin, using HFSB flow tracers. The obtained time-average flow topology matches well to literature, and results obtained at different freestream speeds exhibit the same flow topology, confirming the repeatability of the experiment. During the experiment, the in-house built seeder was traversed into different positions to obtain flow tracers in the full domain. The cameras and laser, instead, always imaged and illuminated the entire measurement region. By invoking the conservation of momentum in a control volume containing the model, the time-average aerodynamic drag acting on the wind tunnel model is expressed as the summation of the momentum, Reynolds stress and pressure terms, respectively. It is found that the latter term is negligible; hence, the pressure reconstruction can be omitted for drag evaluation at a downstream distance of $x/L\geq2.2$, being L the characteristic length of the model, in this case selected as the hip width. Conversely, the momentum term dominates the overall drag force, contributing to about 95% of the drag value. The drag accuracy of the technique is validated against force balance data, from measurements at five freestream velocities. The resulting drag resolution of the PIV wake rake approach is 30 drag counts or $\Delta C_D = 0.03$. Although this qualifies the PIV wake rake as a rather coarse instrument for drag determination, increased accuracy can be expected using a seeding system placed inside the settling chamber of the wind tunnel, which would reduce the induced velocity fluctuations. Additionally, increasing the cross-section of the seeded streamtube would allow a more homogenous seeding concentration and reduce the uncertainty stemming from the displacement of the seeding system.

References

- Agüera N, Cafiero G, Astarita T, Discetti S (2016) Ensemble 3D PTV for high resolution turbulent statistics. Meas. Sci. Technol. 27 124011.
- Alons HJ (2008) OJF External Balance. Nationaal Lucht en Ruimtevaartlaboritorium (National Aerospace Laboratory NLR), NLR-CR-2008-695.
- Barry N, Burton D, Sheridan J, Thompson M, Brown NAT (2014) Aerodynamic performance and riding posture in road cycling and triathlon. Proc IMechE Part P: J Sports Engineering and Technology 1–11.
- Betz A (1925) A method for the direct determination of profile drag (in German). Zeitschrift für Flugtechnik und Motorluftschifffahrt 16:42–44.
- Blocken B, Defraeye T, Koninkx E, Carmeliet J, Hespel P (2013) CFD simulations of the aerodynamic drag of two drafting cyclists. Computers & Fluids 71 435-445.
- Bosbach J, Kühn M, Wagner C (2009) Large scale particle image velocimetry with helium filled soap bubbles. Exp. Fluids 46:539–547. doi:10.1007/ s00348-008-0579-0.
- Caridi GCA, Ragni D, Sciacchitano S, Scarano F (2016) HFSB-seeding for large-scale tomographic PIV in wind tunnels. Exp. Fluids 57:190. doi:10.1007/ s00348-016-2277-7.
- Crouch TN, Burton D, Brown NAT, Thomson MC, Sheridan J (2014) Flow topology in the wake of a cyclist and its effect on aerodynamic drag. J. Fluid. Mech. 748:5–35. doi:10.1017/ jfm.2013.678.
- Crouch TN, Burton D, Thompson MC, Brown NAT, Sheridan J (2016) Dynamic leg-motion and its effect on the aerodynamic performance of cyclists. J. Fl. Str. 65 121-137.
- Goett HJ (1939) Experimental investigation of the momentum method for determining profile drag. NACA Annu. Rep. 25:365–371.
- Grappe F (2009) Resistance totale qui s'oppose au deplacement en cyclisme [Total resistive forces opposed to the motion in cycling]. In Cyclisme et Optimisation de la Performance (2nd edn.) [Cycling and optimisation of performance] (p. 604). Paris: De Boeck Universite´, Collection Science et Pratique du Sport.
- Griffith MD, Crouch T, Thompson MC, Burton D, Sheridan J, Brown NA (2014). Computational fluid dynamics study of the effect of leg position on cyclist aerodynamic drag. J. of Fluids Engineering, 136(10) 101105.
- Hucho W, Sovran G (1993) Aerodynamics of road vehicles. Annu. Rev. Fluid Mech. 25:485–537. doi:10.1146/ annurev.fl.25.010193.002413.
- Jones BM (1936) Measurement of profile drag by the pitot-traverse method. ARC R&M No. 1688.

- Jux C, Sciacchitano A, Schneiders JFG, Scarano F (2018) Robotic volumetric PIV of a full-scale cyclist. Exp. Fluids 59:74. https:/ / doi.org/ 10.1007/ s00348-018-2524-1.
- Kurtulus DF, Scarano F, David L (2007) Unsteady aerodynamic forces estimation on a square cylinder by TR-PIV. Exp. Fluids 42 185–96.
- Lin JC, Rockwell D (1996) Force identification by vorticity fields: techniques based on flow imaging. J. Fluids Struct. 10:663–668.
- Lignarolo LEM, Ragni D, Krishnaswami C, Chen Q, Simão Ferreira CJ, Van Bussel GJW (2014) Experimental analysis of the wake of a horizontal-axis wind-turbine model. Renew. Energy 70:31–46.
- Maskell EC (1973) Progress towards a method for the measurement of the components of the drag of a wing of finite span. RAE technical report 72232.
- Mercker E, Wiedemann J (1996) On the correction of interference effects in open jet wind tunnels. SAE Trans. J. Engines 105 (6), 795–809.
- Raffel M, Willert CE, Scarano F, Kähler CJ, Wereley ST, Kompenhans J (2018) Particle Image Velocimetry – A Practical Guide. Springer International Publishing.
- Ragni D, Ashok A, van Oudheusden BW, Scarano F (2009) Surface pressure and aerodynamic loads determination of a transonic airfoil based on particle image velocimetry. Meas. Sci. Technol. 20 074005.
- Ragni D, van Oudheusden BW, Scarano F (2011) Non-intrusive aerodynamic loads analysis of an aircraft propeller blade. Exp. Fluids. 51 361–71.
- Rival DE, van Oudheusden BW (2017) Load‐estimation techniques for unsteady incompressible flows. Exp0 Fluids 58:20. doi:10.1007/ s00348-017-2304-3.
- Scarano F, Ghaemi S, Caridi GCA, Bosbach J, Dierksheide U, Sciacchitano A (2015) On the use of helium-filled soap bubbles for large-scale tomographic PIV in wind tunnel experiments. Exp. Fluids 56:42. doi:10.1007/ s00348-015-1909-7.
- Schanz D, Gesemann S, Schroeder A (2016) Shake The Box: Lagrangian particle tracking at high particle image densities. Exp. Fluids 57-70.
- Schneiders JFG, Caridi GCA, Sciacchitano A, Scarano F (2016) Large-scale volumetric pressure from tomographic PTV with HFSB tracers. Exp. Fluids 57:164. doi:10.1007/ s00348-016-2258-x.
- Somers DM (1997) Design and Experimental Results for the S809Airfoil. NRELlSR-440-6918.
- Terra W, Sciacchitano A, Scarano F (2017). Aerodynamic drag of a transiting sphere by large-scale tomographic PIV. Exp. Fluids, 58:83. doi: 10.1007/ s00348-017-2331-0.

- Tropea C, Yarin A, Foss JF (2007) Springer handbook of experimental fluid mechanics. Springer, Berlin. ISBN 978-3-540-30299-5.
- Unal MF, Lin JC, Rockwell D (1997) Force prediction by PIV imaging: a momentum based approach. J. Fluids Struct. 11:965–971.
- Van Oudheusden BW, Scarano F, Casimiri EWF (2006) Non-intrusive load characterization of an airfoil using PIV. Exp. Fluids. 40: 988–992. doi:10.1007/ s00348-006-0149-2.
- Van Oudheusden BW (2013) PIV-based pressure measurement. Meas. Sci. Technol. 24 032001. doi:10.1088/ 0957-0233/ 24/ 3/ 032001.
- Van Tubergen J, Verlinden J, Stroober M, Baldewsing R (2017) Suited for performance: fast full-scale replication of athlete with FDM. In Proceedings of SCF '17. Cambridge. MA. USA. June 12-13 2017.
- Westerweel J, Scarano F (2005). Universal outlier detection for PIV data. Exp. in Fluids 39(6):1096-1100. doi:10.1007/ s00348-005-0016-6.
- Zdravkovich MM (1990) Aerodynamic of bicycle wheel and frame. J. Wind Eng. Ind. Aerodyn. 40:55–70. doi:10.1016/ 0167-6105(92)90520-K.